

This is the accepted manuscript made available via CHORUS. The article has been published as:

# Coherent chemistry with THz pulses: Ultrafast field-driven isomerization of LiNC

L. A. Pellouchoud and E. J. Reed

Phys. Rev. A **91**, 052706 — Published 18 May 2015

DOI: [10.1103/PhysRevA.91.052706](https://doi.org/10.1103/PhysRevA.91.052706)

# Coherent Chemistry with THz Pulses: Ultrafast Field-Driven Isomerization of LiNC

L. A. Pellouchoud and E. J. Reed\*

*Department of Materials Science and Engineering, Stanford University, Stanford, CA*

The ability to coherently rearrange structures at the atomic scale is among the grand challenges of physical science. Some of the primary obstacles are non-adiabatic increases in energy, such as intramolecular vibrational relaxation (IVR) and electronic excitations. Motivated by recent advances in strong terahertz (THz) pulse generation, we investigate the potential of THz to circumvent these obstacles. Employing TDDFT-Ehrenfest simulations, we discover that strong THz pulses can drive isomerization of the LiNC molecule over barriers greater than 0.2 eV with very low ionization rates and, in the best case, less than 3 meV of residual excess energy. This work points to new potential to predictively manipulate chemical bonds in molecules and materials.

PACS numbers: 31.15.E-, 31.15.ee, 31.50.Bc, 33.20.-t

Keywords: Coherent Control, Ehrenfest, Density Functional Theory, Molecular Dynamics, Terahertz, Lithium Cyanide

## I. INTRODUCTION

The control of chemical reactions by electric fields has been studied in theory and experiments for decades, with far-reaching implications in industry and fundamental science [1–6]. As materials and molecules are heated, the bonds that rearrange are those associated with the smallest energy barriers. Observed reactions are therefore only a thermally probable subset of the full spectrum of possible reactions. Some proposals to control reactions outside this subset involve employing infrared radiation to resonantly excite specific bonds in the electronic ground state [7, 8]. This approach has proven to be less successful than initially hoped due to intramolecular vibrational relaxation (IVR), in which anharmonic coupling of nuclear vibrations leads to irreversible redistribution of energy among the vibrational modes [9].

Ideally, one would like to be able to rearrange specific bonds, then remove the excess energy to leave the system in a state that will not further react or revert back to the initial state. The possibility of targeting a specific ionic motion has been investigated from a theoretical perspective as early as two decades ago, beginning with model cases where IVR will not take place (e.g. harmonic bonds) [10], but a trajectory that traverses a reaction barrier is sure to deviate from harmonic vibrational regimes. In experimental work, the excitation or cleavage of specific bonds [11, 12], as well as the isomerization, dissociation, or ionization of molecules [13, 14], have been demonstrated by feedback-based optimally controlled strong infrared pulses. Ultrafast IR pulses combined with UV photoexcitations have yielded selective bond breaking [15, 16] as well as control over surface reactions [17, 18], including agreement between modeling and experiments. Optical excitations have also been demonstrated to yield stereoisomer selectivity in complex organic molecules [19]. While the above works

employed pulses of tens or hundred of cycles, we propose to use a nearly single-cycle tailored pulse to circumvent IVR while accomplishing detailed, predictive control over the product structure and temperature. Only recently, with improvements in accelerator-based sources, has it been feasible to study the effects of such strong THz pulses [20]. Because large electric field amplitudes are likely in this approach, we must consider the possibility of electronic excitations and ionization, so we employ semi-classical TDDFT Ehrenfest molecular dynamics to continuously monitor the electronic state.

Inspired by recent technological advances in terahertz (THz) electric field sources, we propose using a strong THz transient to excite and then immediately relax nuclear motions in a near single cycle without excessive heating or ionization of the target. Although THz source capabilities have historically lagged behind their higher and lower frequency counterparts, research in the past several years has yielded progress in the generation and control of THz fields [21–25], and very strong THz sources have been demonstrated recently using particle accelerators [26–28]. THz pulses in refs 27 and 28 are reported to exhibit unprecedented peak amplitudes on the V/Å scale, approaching the fields inside weak chemical bonds. Such advances in THz sources have motivated a variety of studies attempting to use THz radiation to coherently control nuclear and electronic degrees of freedom [29–33].

The sub-picosecond timescale of a THz pulse may enable energy to be pumped into and then out of the system before appreciable IVR occurs. For shorter pulse durations, however, the field amplitudes must be larger in order to drive the ions more quickly, potentially leading to excitation or ionization of electrons. In this work we explore these competing factors in driving transitions between three isomers of the lithium cyanide (LiNC) molecule in semi-classical time-dependent density functional theory (TDDFT) based Ehrenfest dynamics. We simulate the dynamics of LiNC molecules subjected to THz pulses that we have designed to convert the molecule from its lowest energy isomer to the two higher energy isomers while minimizing residual thermal energy and re-

---

\* evanreed@stanford.edu

maining in the electronic ground state.

LiNC has been an attractive subject for computational work, including a coherent control study on longer timescales (hundreds of picoseconds) [34]. Tabulated comparisons of the energetics and structural properties of the three isomers of LiNC by calculations [35–40] as well as experiments [41–43] are included in Appendix A. In ref 43, rotational spectroscopy was used to determine that the most stable structure is linear with Li adjacent to N. Ab-initio calculations predict two other distinct minima, one triangular conformation and one linear with Li adjacent to C. Experiments and computations agree that the bond bending mode of the molecule falls near  $100\text{ cm}^{-1}$ , or approximately 3 THz, while the two stretching modes of the molecule occur near  $700$  and  $2000\text{ cm}^{-1}$ . We attempt to design a THz field pulse that couples specifically to the bending mode to navigate the extrema of the potential surface.

## II. METHODS

A primary challenge in this study is to design an electric field pulse that isomerizes the molecule without leaving excessive residual energy. To accomplish this, we optimize an electric field pulse using a classical mechanical model of LiNC. We then test the optimized electric field pulses within semi-classical TDDFT-based Ehrenfest dynamics. DFT and TDDFT calculations were performed with the Octopus software package, version 4.1.2 [44–46]. DFT calculations include ground-state energies and vibrational frequencies. TDDFT calculations include linear-response electronic excitation spectra and molecular dynamics under applied electric fields. We also used the Gaussian09 software package [47] to compute energies, vibrational frequencies, and TDDFT electronic excitations. See the Appendix for full details of the calculations performed in this work.

### A. Electric Field Pulses for LiNC Isomerization

For deriving the electric field pulses, we employ a model of the LiNC molecule that treats the atoms as classical particles on a DFT-computed field dependent potential surface. We employ a rigid CN bond, reducing the structure to the three coordinates labeled in figure 1 as  $\theta$ ,  $\phi$ , and  $r$ . The potential energy is a function of these coordinates and a time-varying electric field  $\mathbf{E}$ ,  $V = V(r, \theta, \phi, \mathbf{E})$ .

We separate the potential into a zero-field component  $\tilde{V}(r, \theta)$  and an additive field-dependent term  $V_E(r, \theta, \phi, \mathbf{E})$ , such that  $V(r, \theta, \phi, \mathbf{E}) = \tilde{V}(r, \theta) + V_E(r, \theta, \phi, \mathbf{E})$ . Taking the field polarization to be in the molecular plane, suppose that the field-dependent potential  $V_E$  can be approximated by first derivatives in  $\theta$ ,  $\phi$ ,

and  $r$ ,

$$\begin{bmatrix} \frac{\partial V_E}{\partial r} \\ \frac{1}{r} \frac{\partial V_E}{\partial \theta} \\ \frac{1}{r} \frac{\partial V_E}{\partial \phi} \end{bmatrix} = \begin{bmatrix} -q_{rr}(r, \theta) & -q_{r\theta}(r, \theta) \\ -q_{\theta r}(r, \theta) & -q_{\theta\theta}(r, \theta) \\ -q_{\phi r}(r, \theta) & -q_{\phi\theta}(r, \theta) \end{bmatrix} \begin{bmatrix} E_r \\ E_\theta \end{bmatrix}, \quad (1)$$

where  $E_r$  and  $E_\theta$  are the electric field vector components in the molecule reference frame, shown as  $(\hat{\mathbf{r}}, \hat{\theta})$  in figure 1.

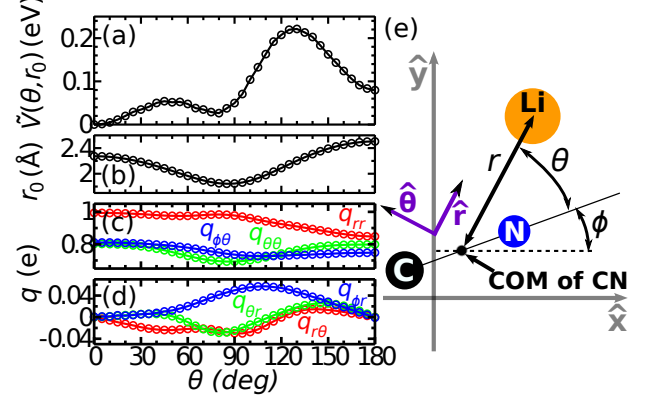


FIG. 1. (color online) a,b: Zero-field potential  $\tilde{V}(\theta, r_0)$  and relaxed radial coordinate  $r_0(\theta)$ . c,d: Force constants of equation 1. e: Reduced coordinates describing lithium cyanide with a rigid CN bond. Coordinates  $r$  and  $\theta$  are defined relative to the center of mass (COM) of the CN group. A laboratory reference frame  $(\hat{\mathbf{x}}, \hat{\mathbf{y}})$  and the molecule reference frame  $(\hat{\mathbf{r}}, \hat{\theta})$  are also defined. Electric fields are applied in the  $(x, y)$  plane.

We computed the relaxed  $r$  coordinate  $r_0(\theta)$  and zero-field potential  $\tilde{V}(r_0, \theta)$  in Octopus by constrained geometry relaxations (see Appendix A). We determined the force constants  $\{q\}$  of equation 1 by applying finite electric fields of  $\pm 0.1\text{ V/\AA}$  with  $r = r_0(\theta)$ , computing the atomic forces, and solving equation 1 for  $q_{rr}$ ,  $q_{r\theta}$ ,  $q_{\theta r}$ ,  $q_{\theta\theta}$ ,  $q_{\phi r}$ , and  $q_{\phi\theta}$ . We then prescribed an isomerization pathway  $\theta(t)$ , with pulse duration  $t_{\text{fin}}$ , isomer geometry  $\theta(t_{\text{fin}}) = \theta_{\text{iso}}$ , and radial constraint  $r(t) = r_0(\theta(t))$ , and solved for a (time-varying) electric field to drive the prescribed  $\theta(t)$  within the field-dependent potential of figure 1. The full derivations of isomerization pathways and electric fields are given in Appendix B.

## III. RESULTS

Beginning with LiNC in its most stable conformation, we performed TDDFT-Ehrenfest simulations with time-dependent pulses designed to drive the molecule from the LiNC conformation to one of the two higher-energy isomer states (see figure 1). A successful isomerization to the triangular conformation is shown in figure 2, with the pulse shape shown in figure 2(a). The molecule ends in the triangle conformation with residual energy of 3 meV, including ionic heating of approximately 3 K.

For a range of the THz pulse duration  $t_{\text{fin}}$ , figure 3 shows the final energy and ionized charge alongside the maximum magnitude and highest-frequency spectral component of the applied fields for pulses targeting both isomers. The highest-frequency spectral component  $\nu_{\text{max}}$  is taken to be

$$\int_0^{\nu_{\text{max}}} |\tilde{\mathbf{E}}(\nu)|^2 d\nu = 0.99 \times \int_0^\infty |\tilde{\mathbf{E}}(\nu)|^2 d\nu. \quad (2)$$

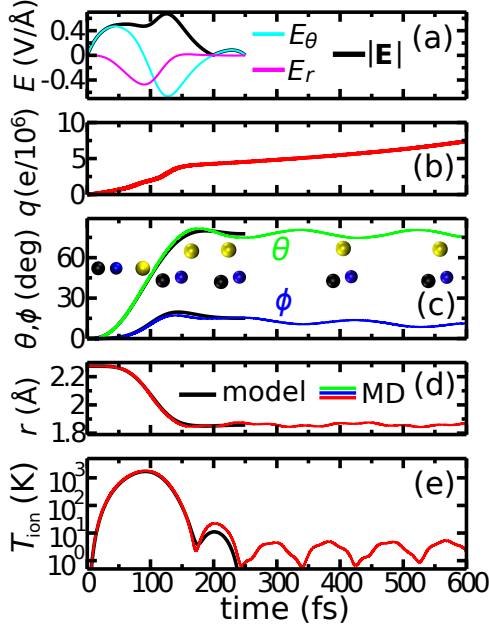


FIG. 2. (color online) TDDFT-Ehrenfest dynamics simulation of a successful field-driven isomerization of Lithium Cyanide to its triangular conformation. a: Applied electric field pulse, with  $t_{\text{fin}} = 250$  fs, derived from equation 7 with the constraints of equations 9 through 11. b: Ionized charge. c: Model trajectories (black) versus TDDFT-Ehrenfest trajectories of  $\theta(t)$  (green) and  $\phi(t)$  (blue), along with snapshots taken at 0, 100, 200, 400, and 600 fs. d: Model trajectory (black) versus TDDFT-Ehrenfest trajectory (red) of  $r(t)$ . e: Ionic temperature,  $T_{\text{ion}} = (2e_{\text{kin}})/(3k_B)$ , based on the model trajectory (black) and TDDFT-Ehrenfest trajectory (red).

Figure 3 shows that our pulses exhibit a range of durations that result in final energies less than the energy required to surmount the transition barrier back to the initial state. For triangle isomerizations (left side), the range is from 200 to 500 fs, while for the linear LiCN isomerizations, the range is from 400 to 900 fs.

The physical mechanisms that result in increased energy at the end of the shortest and longest pulses differ. For the shortest pulse durations  $t_{\text{fin}} < 200$  fs, the closeness of the total energy ( $e_{\text{tot}}$ , blue diamonds) to the total energy less ion kinetic energy ( $e_{\text{tot}} - e_{\text{kin}}$ , blue  $\times$ s) suggests the increase in energy is due to ionization and/or excitation of the electron system, rather than ion kinetic heating. This is what one might naively expect because

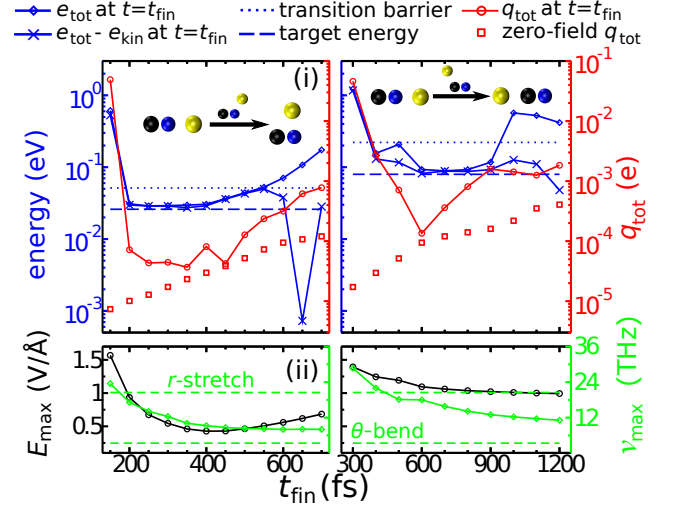


FIG. 3. Left side: LiNC to triangle conformation isomerizations. Right side: LiNC to linear LiCN isomerizations. (i): Final total energy  $e_{\text{tot}}$  (blue diamonds), total energy less ion kinetic energy  $e_{\text{tot}} - e_{\text{kin}}$  (blue  $\times$ s), and ionized charge (red) for different pulse durations. The dotted blue line shows the energy of the transition barrier between the initial (linear LiNC) and target (isomer) states, and the dashed blue line shows the energy of the isomer state. Energies are on the left (blue) axis, and charges are on the right (red) axis. (ii): Maximum field amplitude (black, left axis) and highest-frequency spectral component (green, right axis) for different pulse durations. Green dashed lines show the target bending mode ( $\theta$ -bend) and the radial stretch mode ( $r$ -stretch).

the maximum field magnitudes increase with decreasing  $t_{\text{fin}}$ . At longer pulse durations  $t_{\text{fin}} > 500$  fs, more ion kinetic energy is imparted by the pulse, as is evident where these two curves separate. The excess ion kinetic energy at longer durations is likely due to limitations of the model used to generate the pulses as well as some amount of IVR. The least excess energy is achieved for the triangle case at  $t_{\text{fin}} = 250$  fs (less than 0.003 eV), and for the LiCN case at  $t_{\text{fin}} = 700$  fs (less than 0.010 eV).

From an experimental perspective, molecular orientation relative to the applied field will have a strong influence on the success of isomerization. Indeed, the control of molecular orientation with electric fields has been demonstrated and refined in experimental settings for over 15 years [48–54]. We investigate the effect of orientation misalignment by applying the pulse shown in figure 2 (targeting the triangle isomer) to a molecule rotated by first by  $\phi_0$  in the  $xy$  plane and then by  $\beta_0$  about the  $y$  axis (see the coordinates of figure 1), while the field polarization remains in the  $xy$  plane. According to figure 4, the range of orientations that result in final energies below the 0.051 eV transition barrier encompass 0.7% of all possible orientations. To perform an analogous process in a laboratory setting, methods of introducing molecular alignment (as in refs 48–54) may be important for achieving high isomerization yields.

To clarify how the field couples to the molecule, fig-

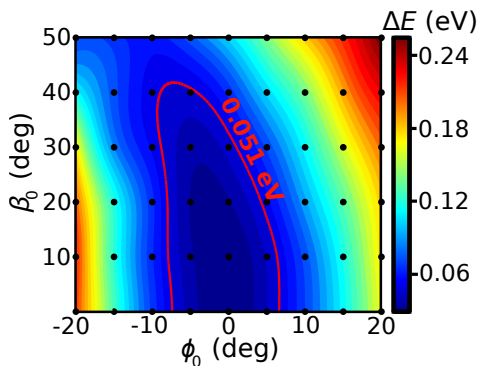


FIG. 4. (color online) Final total energy and ionized charge for different initial molecular orientations under the isomerization pulse shown in figure 2 panel (a). Orientations within the region outlined in red isomerize to the triangular conformation with insufficient residual energy to surmount the 0.051 eV barrier. Sampled points are marked by black dots, and the surface is interpolated by a 2-dimensional cubic spline.

Figure 5 shows the vibrational spectra (by Octopus Sternheimer linear response) and electronic excitation spectra (by Octopus linear response time-domain TDDFT) of the three isomers, along with the spectral energy density of the applied field. The electric field pulses align with the bending (lowest frequency) mode, with very little overlap on the other two modes that correspond to Li stretch and CN stretch modes. Electronic excitations occur at frequencies significantly higher than any of the E-field or ionic features. Further details of the vibrational and electronic frequencies are included in Appendix A.

## IV. DISCUSSION

### A. Mechanisms limiting coherence

Several mechanisms can limit the range of pulses that successfully isomerize the molecule, including the coupling of energy into degrees of freedom from which it cannot be removed, such as electronic excitation (or ionization) and IVR. Figure 3 suggests electronic effects impose a lower limit on pulse duration, while nuclear heating (due to imperfect pulse shapes and potentially IVR) precludes isomerization for long durations. The bottom panels of Figure 3 suggest direct excitation of the Li stretch mode may also play a role.

To design the THz pulses used in this work, we employed several approximations that are likely to play a role in decoherence. The approximation of field-induced forces (equation 1) introduces an error source that is likely to increase with the pulse amplitude. Variations of the  $r$  coordinate away from  $r_0(\theta)$  will give rise to a more complicated source of error. Variations in  $r$  instigate deviation from the potential surface  $\tilde{V}(r_0, \theta)$  used to derive the pulses, and also compound the error in the forces of equation 1 because the force constants  $\{q\}$  were deter-

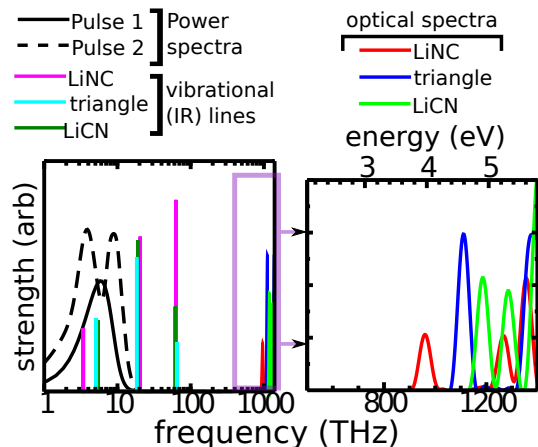


FIG. 5. (color online) Computed vibrational frequencies and TDDFT electronic excitation spectra for the three stable isomers, along with spectral power densities of isomerization pulses. Pulse 1 is the 250 fs isomerization pulse shown in figure 2, and pulse 2 is the 700 fs pulse targeting the LiNC to linear LiCN isomerization. The bandwidth of these pulses overlaps primarily with the 3-6 THz molecular bending mode and exhibits little overlap with higher frequency vibrations. The plotted electronic spectra in this figure have been truncated below the first excitation peak to remove Fourier transform artifacts.

mined using  $r = r_0(\theta)$ . The highly nonlinear physics of isomerization under such strong fields may allow these errors to amplify in relatively short time periods. Although more accurate models are conceivable, the present work clearly demonstrates the feasibility of designing isomerizing pulses even at the present level of refinement.

### B. Conclusions

We have demonstrated classically coherent, non-destructive control of molecular isomerization reactions by THz electric field pulses using semi-classical TDDFT Ehrenfest dynamics. We employed LiNC as a simple test case that exhibits distinct stable structures. We find that it is possible to achieve isomerization over a barrier of 0.051 eV (triangle conformation) with excess energy of less than 0.003 eV, and over a barrier of 0.22 eV (linear LiCN conformation) with excess energy of less than 0.01 eV.

We find that electronic excitation/ionization imposes a lower limit on the pulse duration for successful isomerization, while unintended vibrational energy redistribution limits coherence at longer durations, likely due to imperfections in the pulse shape and some amount of IVR. While IVR may be expected to preclude coherent isomerization for pulses of sufficiently long duration, our observed increase in residual energy for longer durations does not suggest that isomerization cannot be performed with pulses longer than those studied here. A less simpli-

fied field-dependent potential surface or a feedback-based optimal pulse tailoring scheme may yield improved results for pulses of longer duration. This additional complexity requirement indicates that longer pulses will be more sensitive to the details of the potential surface, and so are likely to be more challenging to design.

## 1. Appendix A: Computational Details

Below, we present details of all the computations performed in this work, for clarity to the point of reproducibility. We also present a comparison of our results against previous computational work [35–40] and available experiments [41–43].

Our primary tool for this work is the Octopus software package, version 4.1.2 [44–46]. For treatment of electronic exchange and correlation (XC) effects in Octopus, we used the local density approximation (LDA) functional attributed to Perdew and Zunger (PZ) [55]. We used the default set of norm-conserving Troullier-Martins pseudopotentials [56] from the library included with the Octopus code. Potentials for C and N were generated with the PZ XC functional, while the potential for Li was generated with the PBE [57] XC functional. Li, N, and C pseudo-atoms include 1, 5, and 4 valence states, respectively. Potentials include two angular momentum components  $l = \{0, 1\}$ , with  $l = 1$  as the local potential. Octopus performs DFT computations with a real-space grid, where wavefunctions are defined by their values at a discrete set of points in space. We employed a cubic grid with a spacing of 0.1 Å between points within a spherical boundary of radius 8 Å (2,433,121 mesh points). A small net force on the molecule may be expected. With this choice of grid parameters, we find the net force on the molecule to be less than  $5\text{E-}5$  Ha/ $a_0$  at all of the critical points on the potential energy surface (PES).


We performed additional calculations using Gaussian 09, Revision B.01 [47], including energies, vibrational frequencies, and TDDFT electronic excitation frequencies at critical points on the PES. For Gaussian calculations, we employed several electronic structure methods, including the SVWN LDA attributed to Slater [58] and Vosko, Wilk, and Nusair [59], the BLYP GGA composed of Becke’s 1988 exchange functional [60] and the correlation functional of Lee, Yang, and Parr [61], the commonly used hybrid B3LYP composed of the same functionals [62], MP4(SDTQ) perturbation theory [63], and quadratic CI with single and double excitations (QCISD) [64]. The Gaussian TDDFT calculations employ the frequency-domain linear response method of Casida [65]. We used the large 6-311+G(2df) basis set [66] for all Gaussian calculations. Electronic structure, ionic relaxation, and linear response TDDFT calculations with Gaussian utilized the default convergence parameters implemented in the Gaussian code.

For Octopus calculations, electronic convergence was determined by a threshold on the change in electron

density between self-consistent field (SCF) iterations, whereby the SCF cycle was stopped when  $1/N_e \times \int d^3\mathbf{r} |\rho_{\text{in}}(\mathbf{r}) - \rho_{\text{out}}(\mathbf{r})| \leq 1\text{E-}5$  e. Geometry relaxations were performed with conjugate-gradient descent, and critical points on the potential surface were taken to be converged when changes in all atomic positions between descent iterations fell below  $1\text{E-}6$   $a_0$  or all forces fell below  $1\text{E-}6$  Ha/ $a_0$ . Using the relaxed geometries, we employed Octopus Sternheimer self-consistent linear response to compute vibrational spectra and linear response time-domain TDDFT to compute optical spectra. We also used a home-built script to interact with Octopus and perform constrained geometry relaxations, to find the minimum-energy  $r$  coordinate at constrained values of  $\theta$  with  $\phi = 0$  and the CN bond relaxed. For these calculations, the radial force component on the Li ion was relaxed to less than  $1\text{E-}6$  Ha/ $a_0$ .

In tables I and II, we show the structural properties and energetics of LiNC based on our calculations (Octopus as well as Gaussian), previously published computations [35–40], and experiments [41–43].

TABLE I. Computed total energies (eV) at key points on the LiNC potential surface. Energies of stable points and transition states were computed with Octopus (PZ-LDA), and energies of stable points were computed with several other electronic structure methods using Gaussian. Unless noted otherwise, calculations were performed with Gaussian and the 6-311+G(2df) basis set. Also shown are data from other reported computations (refs 35, 37, 38).



	LiNC	TS1	tri	TS2	LiCN
Octopus PZ-LDA	0	0.0514	0.0260	0.221	0.0796
SVWN-LDA	0	–	8.71E-4	–	0.0878
BLYP-GGA	0	–	0.0478	–	0.0995
B3LYP	0	–	0.0567	–	0.135
MP4(SDTQ)	0	–	9.01E-4	–	0.0708
QCISD	0	–	0.0216	–	0.115
SVWN-LDA [35]	0	–	0.00103	0.214	0.182
BLYP-GGA [35]	0	–	0.0479	0.245	0.207
B3LYP [35]	0	–	0.0532	0.271	0.237
6-311+G* MP4 [37]	0.035	–	0	–	0.097
6-31+G* MP2 [37]	0.173	–	0	–	0.113
TZ2P MRCISD [38]	0	–	0.026	–	0.094

A DFT-relaxed LiNC molecule was used as the starting point for all time-domain TDDFT calculations, which were performed with the same basis set, pseudopotentials, and (adiabatic) XC functionals as were used to compute the ground state. We employed a time-reversible exponential-midpoint propagator [67] for all TDDFT simulations. The exponential of the Hamiltonian for the propagator was approximated within a 50-dimensional Krylov subspace (10 times the dimensionality of the 5

TABLE II. Bond lengths ( $\text{\AA}$ ) and bending or orbital mode frequencies ( $\text{cm}^{-1}$ ) of LiNC. Values are reported from Octopus (PZ-LDA) as well as Gaussian (several electronic structure methods). Also shown are data from experiments (refs 42, 43) and other computations (refs 35, 37, 38) where available. Unless noted otherwise, calculations were performed with Gaussian and the 6-311+G(2df) basis set.

	$d_{CN}$	$d_{LiN}$	$\nu_{LiNC}$	$\nu_{tri}$	$\nu_{LiCN}$
Experiments [42, 43]	1.168	1.760	119-138 <sup>a</sup>	—	—
Octopus PZ-LDA	1.174	1.732	114	181	171
SVWN-LDA	1.173	1.748	113	203	170
BLYP-GGA	1.183	1.770	117	160	171
B3LYP	1.172	1.760	119	143	175
MP4(SDTQ)	1.190	1.786	77.6	184	165
QCISD	1.177	1.781	90.2	163	172
SVWN-LDA [35]	1.173	1.748	—	—	—
BLYP-GGA [35]	1.183	1.769	—	—	—
B3LYP [35]	1.172	1.760	—	—	—
6-31+G* MP2 [37]	1.196	1.800	—	—	—
TZ2P MRCISD [38]	1.169	1.794	157	—	—

<sup>a</sup> Frequencies for matrix-isolated isotopes in Ar and Ne.

occupied eigenstates) [68].

For the TDDFT-based molecular dynamics simulations where we investigate molecular misalignment (figure 4), we employed the modified Ehrenfest scheme introduced by Andrade, et al, which uses an ionic time scaling factor to reduce computation CPU time [69]. The electronic time step  $dt$  and ionic time scaling  $f_{ITS}$  must be tested for convergence of system dynamics. The equations of TDDFT Ehrenfest dynamics are recovered in the case of  $f_{ITS} = 1$ , while ref 69 concludes that values on the order of 10 are often sufficient to conserve dynamics. We used the isomerizing electric field of figure 2 to check the convergence of the overall ionic trajectory with respect to  $dt$  and  $f_{ITS}$ . We computed trajectories with this field for timesteps as small as  $dt = 0.0015 \hbar/\text{eV}$  (0.001 fs) and as large as  $dt = 0.009 \hbar/\text{eV}$  ( $dt = 0.006$  fs), with  $f_{ITS}$  values from 1 to 40. Simulations with time steps larger than 0.006 fs fail to converge the Krylov subspace exponential of the Hamiltonian for the propagation operator. The trajectories for several time steps and ionic time scaling factors are shown in figure 6. Based on these results, the ionic trajectory appears to be insensitive to electronic time step within the range of time steps that allow the propagator to converge. A moderate ionic time scaling factor (e.g.  $f_{ITS} = 5$ ) yields a trajectory that is indiscernibly different from Ehrenfest dynamics, while an unusually large factor ( $f_{ITS}=40$ ) qualitatively alters the dynamics.

Let  $\{r'(t), \theta'(t), \phi'(t)\}$  denote the trajectory with the smallest time step (0.0015  $\hbar/\text{eV}$ , about 0.001 fs) and  $f_{ITS} = 1$  (Ehrenfest dynamics). A time step of  $dt = 0.0045 \hbar/\text{eV}$  (about 0.003 fs) with  $f_{ITS} = 5$  (for an ef-

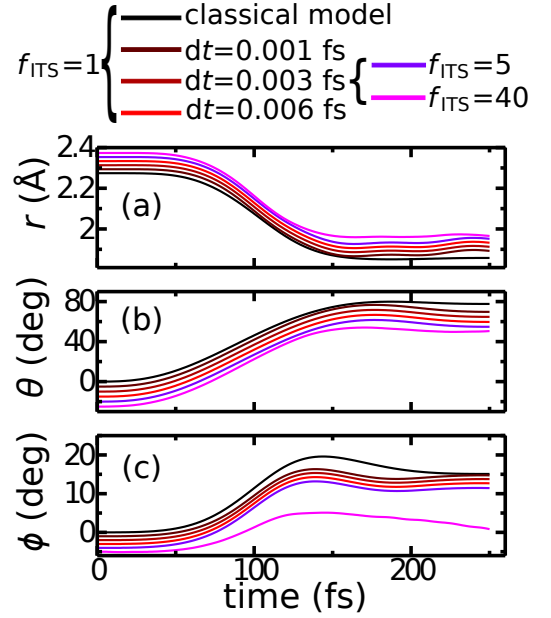


FIG. 6. TDDFT Ehrenfest dynamics compared with classical model prediction for the isomerizing electric field pulse of figure 2 with different electronic time step ( $dt$ ) and ionic time scaling ( $f_{ITS}$ ) values. The model trajectory (black) is the intended path based on the prescription of equation 7, which should not be expected to coincide with the converged TDDFT-Ehrenfest path. The simulated trajectory with the smallest attempted time step (0.001 fs) is different from the model due to inherent differences between the model and the TDDFT simulations (see Discussion section). Larger time steps of  $dt = 0.003$  fs and  $dt = 0.006$  fs, as well  $dt = 0.003$  fs with  $f_{ITS} = 5$ , all yield indistinguishable trajectories. Curves are offset for clarity by 2 degrees in  $\theta$ , 1 degree in  $\phi$ , and 0.01  $\text{\AA}$  in  $r$ . Ionic time scaling error begins to appear for larger  $f_{ITS}$  values, as evidenced by the trajectory with  $f_{ITS} = 40$  and  $dt = 0.003$  fs (magenta).

fective time step of  $dt_{\text{eff}} = 0.0225 \hbar/\text{eV}$ , or about 0.015 fs) result in maximum relative errors in  $r$ ,  $\theta$ , and  $\phi$  of  $|r - r'| < 5E-4 a_0$ ,  $|\phi - \phi'| < 0.3^\circ$ , and  $|\theta - \theta'| < 0.1^\circ$ . Because these errors are small relative to the changes in coordinates over the trajectory, we have used  $dt = 0.003$  fs for all of the TDDFT dynamics presented in this work. In the study of molecular orientation (figure 4), we employ an ionic time scaling factor  $f_{ITS} = 5$ .

To approximately simulate strong-field ionization of the molecule in real-time TDDFT, we applied an absorbing boundary region to the simulation mesh. The absorbing boundary modifies the Kohn-Sham potential  $V_{KS}$  by an imaginary term  $iV_{\text{abs}}$  that is confined to the region near the boundary of the simulation box,  $V_{\text{tot}} = V_{KS} - iV_{\text{abs}}$ . Defining  $\mathbf{r} \leq \mathbf{r}_b$  to be a radial coordinate of the spherical simulation mesh, we use an absorbing boundary of

$$V_{\text{abs}}(\mathbf{r}) = \begin{cases} 0, & |\mathbf{r}_b - \mathbf{r}| > 0.4a_0 \\ \sin^2\left(\pi \frac{|\mathbf{r}_b - \mathbf{r}|}{0.4a_0}\right) \times 0.2\text{Ha}, & |\mathbf{r}_b - \mathbf{r}| \leq 0.4a_0 \end{cases}.$$

Wavefunction components that reside in the absorbing region evidently become attenuated in magnitude under the Kohn-Sham propagation operator  $\hat{U}(t, 0) = \mathcal{T} \exp \left( -i \int_0^t \hat{H}_{\text{KS}}(\tau) d\tau \right)$ , where  $\mathcal{T} \exp$  denotes a time-ordered (non-commutable) exponential. In the case of an absorbing potential, charge conservation under propagation is not required, and we observe a slow leakage of charge from the system at a rate of about 1E-7 e/fs with  $dt = 0.003$  fs,  $f_{\text{ITS}} = 1$  (Ehrenfest dynamics), and no applied field. Ionic time scaling of  $f_{\text{ITS}} = 5$  slows the ionization rate to about 1E-8 e/fs. Because ionic time scaling affects the ionization behavior of the molecule, we do not use ionic time scaling for simulations where field-induced ionization may play a role.

Linear-response TDDFT optical spectra were computed at critical points on the PES by applying a time-domain delta-function electric field and propagating the wavefunctions through time, and then taking the Fourier transform of the time-dependent dipole moment of the molecule. For a delta-function electric field of strength  $\kappa$  in the  $\mathbf{x}$  direction, an initial phase factor of  $\exp(i\kappa\mathbf{x})$  is imparted to the wavefunctions. In other words, for a ground-state Kohn-Sham wavefunction  $\psi_{\text{GS}}$ , the initial value of the wavefunction for the optical spectrum propagation is  $\psi_{\text{TD}}(0) = \psi_{\text{GS}} \exp(i\kappa\mathbf{x})$ . We employed a delta-function electric field strength of  $\kappa = 2\text{E-4 a}_0^{-1}$  and an electronic time step of 0.003  $\hbar/\text{eV}$  (0.002 fs) for 10000 steps (about 20 fs total). With this time step and duration, the lowest and highest discernible frequency components are expected to be about 0.2 eV and 1 keV, respectively. The field was applied separately in three orthogonal polarizations to build the full (complex) linear susceptibility tensor  $\chi_{\alpha\beta}(\omega)$ . We then report the absorption cross section as  $\sigma(\omega) = \text{Tr}[2\omega/(3\pi) \times \chi_{\alpha\beta}(\omega)]$ . For validation purposes, the Octopus absorption peaks from figure 5 are compared against Gaussian09 frequency-domain TDDFT excitations with three different exchange and correlation (XC) functionals in table III below.

TABLE III. Lowest-energy absorption peak (in eV) of the three isomers of LiNC with several TDDFT methods. The trend in peak locations between isomers is consistent between all methods and indicates the potential for a UV probe to determine the conformation. Octopus real-time TDDFT calculations are plotted in figure 5. Gaussian TDDFT calculations use the frequency-domain method of Casida [65] and were performed with the 6-311+G(2df) basis set.

	LiNC tri LiCN		
Octopus PZ-LDA	4.0	4.6	4.9
Gaussian SVWN-LDA	3.9	4.6	4.8
Gaussian BLYP-GGA	3.2	3.9	4.1
Gaussian B3LYP	4.2	4.7	5.1

## 2. Appendix B: Derivation of Electric Field Pulses for Isomerization

The potential energy of the classical LiNC model used in this work is a function of  $r$ ,  $\theta$ ,  $\phi$ , and a time-dependent electric field  $\mathbf{E}(\mathbf{t})$  polarized in the molecular plane,  $V = V(r, \theta, \phi, \mathbf{E})$ . Defining a reduced mass  $\mu = (m_{\text{Li}}m_{\text{CN}})/(m_{\text{Li}} + m_{\text{CN}})$  and a rotational moment of inertia for cyanide  $I = d_{\text{CN}}^2(m_{\text{C}}m_{\text{N}}^2 + m_{\text{N}}m_{\text{C}}^2)/(m_{\text{N}} + m_{\text{C}})^2$ , the kinetic energy is

$$T = \frac{1}{2} \left( \mu \dot{r}^2 + \mu r^2 (\dot{\theta} + \dot{\phi})^2 + I \dot{\phi}^2 \right) \quad (3)$$

We approximate the CN bond to be rigid. The relaxed CN bond ranges from 1.163 Å ( $\theta = 180^\circ$ ) to 1.176 Å ( $\theta \approx 55^\circ$ ). We use the average value with respect to  $\theta$ , 1.171 Å. The dynamics for a set of generalized coordinates  $\{s\}$  can be predicted via the Euler-Lagrange equations,

$$L = T - V, \\ \frac{d}{dt} \left( \frac{\partial L}{\partial \dot{s}} \right) = \frac{\partial L}{\partial s}.$$

Applying the Euler-Lagrange equations for  $r$ ,  $\theta$ , and  $\phi$  leads to a set of coupled second-order differential equations:

$$\ddot{r} = r (\dot{\theta} + \dot{\phi})^2 - \frac{1}{\mu} \frac{\partial V}{\partial r}, \\ \ddot{\theta} = \frac{1}{I} \left( \frac{\partial V}{\partial \theta} - \frac{\partial V}{\partial \phi} \right), \\ \ddot{\phi} = \frac{1}{\mu r^2} \left( -2\mu r \dot{r} (\dot{\theta} + \dot{\phi}) - \frac{\partial V}{\partial \theta} \right) - \frac{1}{I} \left( \frac{\partial V}{\partial \theta} - \frac{\partial V}{\partial \phi} \right). \quad (4)$$

To accomplish coherent control, we aim to prescribe a trajectory in the relevant coordinates and find a time-varying electric field that drives the system along that trajectory without causing excessive heating or ionization. For coherent isomerization of LiNC, one way to do this is to prescribe  $\theta(t)$  and  $r(t)$  such that the molecule begins in its most stable conformation and ends in a distinct metastable conformation.

We separate the potential energy into a zero-field component  $\tilde{V}(r, \theta)$  and an additive field-dependent term,  $V_E(r, \theta, \phi, \mathbf{E})$ ,

$$V(r, \theta, \phi, \mathbf{E}) = \tilde{V}(r, \theta) + V_E(r, \theta, \phi, \mathbf{E}), \\ \frac{\partial V}{\partial \theta} = \frac{\partial \tilde{V}}{\partial \theta} + \frac{\partial V_E}{\partial \theta}, \\ \frac{\partial V}{\partial \phi} = \frac{\partial V_E}{\partial \phi}, \\ \frac{\partial V}{\partial r} = \frac{\partial \tilde{V}}{\partial r} + \frac{\partial V_E}{\partial r}.$$

In this case, equation 4 becomes

$$\begin{aligned}
\ddot{\theta} &= \frac{1}{\mu r^2} \left( -2\mu r \dot{r} (\dot{\theta} + \dot{\phi}) - \frac{\partial \tilde{V}}{\partial \theta} - \frac{\partial V_E}{\partial \theta} \right) \\
&\quad - \frac{1}{I} \left( \frac{\partial \tilde{V}}{\partial \theta} + \frac{\partial V_E}{\partial \theta} - \frac{\partial V_E}{\partial \phi} \right), \\
\ddot{\phi} &= \frac{1}{I} \left( \frac{\partial \tilde{V}}{\partial \theta} + \frac{\partial V_E}{\partial \theta} - \frac{\partial V_E}{\partial \phi} \right), \\
\ddot{r} &= r (\dot{\theta} + \dot{\phi})^2 - \frac{1}{\mu} \left( \frac{\partial \tilde{V}}{\partial r} + \frac{\partial V_E}{\partial r} \right). \tag{5}
\end{aligned}$$

For the field amplitudes of interest here, we suppose that the derivatives of the field-dependent potential  $V_E$  may be approximated to first order in  $\theta$ ,  $\phi$ , and  $r$  as

$$\begin{aligned}
\frac{\partial V_E}{\partial r} &= -q_{rr} E_r - q_{r\theta} E_\theta, \\
\frac{1}{r} \frac{\partial V_E}{\partial \theta} &= -q_{\theta r} E_r - q_{\theta\theta} E_\theta, \\
\frac{1}{r} \frac{\partial V_E}{\partial \phi} &= -\frac{1}{r} \tau_z = -q_{\phi r} E_r - q_{\phi\theta} E_\theta. \tag{6}
\end{aligned}$$

where  $\tau_z$  is the component of the overall torque vector normal to the plane of the molecule, and  $E_r$  and  $E_\theta$  are the components of the electric field vector in the molecule reference frame. Note that this is an expansion of the tensor form shown in equation 1. This approximation of the field-dependent potential amounts to computing the effect of the applied field on each of the degrees of freedom represented by the reduced coordinates.

Plugging equation 6 into equation 5 gives

$$\begin{aligned}
\ddot{\theta} &= \frac{1}{\mu r^2} \left( -2\mu r \dot{r} (\dot{\theta} + \dot{\phi}) - \frac{\partial \tilde{V}}{\partial \theta} + r q_{\theta\theta} E_\theta + r q_{\theta r} E_r \right) \\
&\quad - \frac{1}{I} \left( \frac{\partial \tilde{V}}{\partial \theta} - r q_{\theta\theta} E_\theta - r q_{\theta r} E_r + r q_{\phi\theta} E_\theta + r q_{\phi r} E_r \right), \\
\ddot{\phi} &= \frac{1}{I} \left( \frac{\partial \tilde{V}}{\partial \theta} - r q_{\theta\theta} E_\theta - r q_{\theta r} E_r + r q_{\phi\theta} E_\theta + r q_{\phi r} E_r \right), \\
\ddot{r} &= r (\dot{\theta} + \dot{\phi})^2 - \frac{1}{\mu} \left( \frac{\partial \tilde{V}}{\partial r} - q_{rr} E_r - q_{r\theta} E_\theta \right).
\end{aligned}$$

Recall that we wish to prescribe a path in  $\theta(t)$  and  $r(t)$  to accomplish isomerization, and the applied field will have two components,  $E_r$  and  $E_\theta$ . We can choose to rearrange the above equations to solve for  $E_r$  and  $E_\theta$  from the prescribed  $r(t)$  and  $\theta(t)$ , while  $\phi(t)$  evolves col-

laterally:

$$\begin{aligned}
\begin{bmatrix} E_r \\ E_\theta \end{bmatrix} &= B^{-1} \begin{bmatrix} \mu \ddot{r} - \mu r (\dot{\theta} + \dot{\phi})^2 + \frac{\partial \tilde{V}}{\partial r} \\ \mu r \ddot{\theta} + 2\mu \dot{r} (\dot{\theta} + \dot{\phi}) + \frac{\partial \tilde{V}}{r \partial \theta} + \frac{\mu r^2}{I} \frac{\partial \tilde{V}}{r \partial \theta} \end{bmatrix}, \\
B &= \begin{bmatrix} q_{\theta r} + \frac{\mu r^2}{I} q_{\theta r} - \frac{\mu r^2}{I} q_{\phi r} & q_{\theta\theta} + \frac{\mu r^2}{I} q_{\theta\theta} - \frac{\mu r^2}{I} q_{\phi\theta} \end{bmatrix}, \\
\ddot{\phi} &= \frac{1}{I} \left( \frac{\partial \tilde{V}}{\partial \theta} - r q_{\theta\theta} E_\theta - r q_{\theta r} E_r + r q_{\phi\theta} E_\theta + r q_{\phi r} E_r \right). \tag{7}
\end{aligned}$$

Provided the matrix inverse on the right hand side exists, we can find some  $E_r$  and  $E_\theta$  that drives the prescribed  $\theta(t)$  and  $r(t)$ , while the trajectory of  $\phi(t)$  will be solved by integrating an ordinary differential equation. We integrate the equation for  $\phi(t)$  by a 4th-order Runge-Kutta scheme which uses a 5th-order solution to estimate the 4th-order error [70].

Application of equation 7 requires *a priori* knowledge of the  $\theta$ -dependent force constants  $\{q\}$ . We compute them by applying finite electric fields at the radially relaxed geometries for  $\theta$  values from  $0^\circ$  to  $180^\circ$  (by  $5^\circ$  intervals) and finding the force on the Li atom (for  $q_{rr}$ ,  $q_{r\theta}$ ,  $q_{\theta r}$ , and  $q_{\theta\theta}$ ) and overall torque on the molecule (for  $q_{\phi r}$  and  $q_{\phi\theta}$ ) with these finite fields. In particular,

$$\begin{aligned}
q_{rj}(\theta) &= \frac{F_r^{\text{Li}}(\theta, E_j^+) - F_r^{\text{Li}}(\theta, E_j^-)}{E_j^+ - E_j^-}, \\
q_{\theta j}(\theta) &= \frac{F_\theta^{\text{Li}}(\theta, E_j^+) - F_\theta^{\text{Li}}(\theta, E_j^-)}{E_j^+ - E_j^-}, \\
q_{\phi j}(\theta) &= \frac{\tau_z(\theta, E_j^+) - \tau_z(\theta, E_j^-)}{r_0(\theta)(E_j^+ - E_j^-)}. \tag{8}
\end{aligned}$$

We used applied field amplitudes of  $E_j^\pm = \pm 0.1$  V/Å to extract the constants used in this work. The results are shown in figure 1.

The first step in applying this model is to prescribe a path  $\theta(t)$ ,  $r(t)$  that accomplishes isomerization. For a given duration  $t_{\text{fin}}$ , isomerization requires the following boundary conditions on  $\theta(t)$ :

$$\begin{aligned}
\theta(0) &= \dot{\theta}(0) = \ddot{\theta}(0) = 0, \\
\theta(t_{\text{fin}}) &= \theta_{\text{iso}}, \\
\dot{\theta}(t_{\text{fin}}) &= \ddot{\theta}(t_{\text{fin}}) = 0. \tag{9}
\end{aligned}$$

Meanwhile, we may choose  $r(t)$  to follow the radial minimum in  $\theta$ , such that

$$\begin{aligned}
\frac{\partial \tilde{V}}{\partial r} &= 0, \\
r(t) &= r_0(\theta(t)), \\
\dot{r} &= \frac{dr_0}{d\theta} \dot{\theta}, \\
\ddot{r} &= \frac{d^2 r_0}{d\theta^2} \dot{\theta}^2 + \frac{dr_0}{d\theta} \ddot{\theta}. \tag{10}
\end{aligned}$$

With this constraint on  $r(t)$ , it is ensured that the initial and final states have no velocity or acceleration in  $r$  as long as the constraints on  $\theta(t)$  are satisfied. We employed this choice to simplify the consideration of the potential surface, though variations in  $r$  away from  $r_0$  may yield increased optimality (e.g. isomerization pathways with smaller electric field amplitudes).

We satisfied the six constraints on  $\theta(t)$  by choosing  $t_{\text{fin}}$  and solving for the unique 5th-order polynomial that satisfies all six conditions.

$$\theta(t) = a_0 + a_1 t + a_2 t^2 + a_3 t^3 + a_4 t^4 + a_5 t^5.$$

Additionally, to ensure the final isomer is cold and  $\mathbf{E}(t_{\text{fin}}) = 0$ , we require

$$\dot{\phi}(t_{\text{fin}}) = 0. \quad (11)$$

(see equations 3 and 7). This condition is met by augmenting the polynomial for  $\theta(t)$  to sixth order and searching the space of polynomial coefficients  $\{a\}$  that satisfy the boundary conditions on  $\theta(t)$  (equation 9) to find a polynomial for that also satisfies equation 11. This is a complicated nonlinear constraint because  $\phi(t)$  must be integrated numerically. We find trajectories that satisfy equations 9 and 11 by a Nelder-Mead simplex search [71] over the coefficients  $\{a\}$  for all electric field pulses presented in this study. Further optimization of the electric field is possible by augmenting the polynomial to still

higher orders. For pulses targeting the linear LiCN isomer, in which field amplitudes can be large enough to appreciably ionize the molecule, we have augmented the polynomial to seventh order and attempted to minimize the maximum field amplitude in the coefficient space where all of the constraints on  $\theta(t)$  and  $\dot{\phi}(t_{\text{fin}})$  are satisfied. To do this, we solve

$$\min_{\{a\}} \left[ \max_t [|\mathbf{E}(t)|^2] \right]$$

under the (nonlinear) constraints of equations 9 and 11 by an interior-point search [72] over the polynomial coefficients  $\{a\}$ .

## ACKNOWLEDGMENTS

This work was performed at Stanford University and supported by NASA NSTRF Grant NNX12AM48H. Parts of this work utilized resources from the National Energy Research Scientific Computing Center (NERSC), supported by the Office of Science and the U.S. Department of Energy under Contract No. DE-AC02-05CH11231. We gratefully acknowledge discussions and editorial work by Y. Li, Y. Shen, and K.-A. Duerloo, as well as discussions, preliminary calculations, and conceptual work by M. T. Ong, T. Qi, and T. Seletskaja.

- 
- [1] P. Brumer and M. Shapiro, Annual Review of Physical Chemistry **43**, 257 (1992).
  - [2] D. Gruner, P. Brumer, and M. Shapiro, The Journal of Physical Chemistry **96**, 281 (1992).
  - [3] M. Shapiro and P. Brumer, Reports on Progress in Physics **66**, 859 (2003).
  - [4] M. Dantus and V. V. Lozovoy, Chemical Reviews **104**, 1813 (2004).
  - [5] P. Nuernberger, G. Vogt, T. Brixner, and G. Gerber, Physical Chemistry Chemical Physics **9**, 2470 (2007).
  - [6] C. Brif, R. Chakrabarti, and H. Rabitz, New Journal of Physics **12**, 075008 (2010).
  - [7] N. Bloembergen and E. Yablonovitch, Physics Today **31**, 23 (1978).
  - [8] O. Skocek, C. Uiberacker, and W. Jakubetz, The Journal of Physical Chemistry A **115**, 7127 (2011).
  - [9] M. Gruebele, Theoretical Chemistry Accounts **109**, 53 (2003).
  - [10] J. G. B. Beumee and H. Rabitz, Journal of Mathematical Physics **31**, 1253 (1990).
  - [11] R. J. Levis, G. M. Menkir, and H. Rabitz, Science **292**, 709 (2001).
  - [12] R. J. Levis and H. A. Rabitz, The Journal of Physical Chemistry A **106**, 6427 (2002).
  - [13] O. Khn, J. Manz, and Y. Zhao, Physical Chemistry Chemical Physics **1**, 3103 (1999).
  - [14] C. M. Tesch, K.-L. Kompa, and R. d. Vivie-Riedle, Chemical Physics **267**, 173 (2001).
  - [15] N. Elghobashi, P. Krause, J. Manz, and M. Oppel, Physical Chemistry Chemical Physics **5**, 4806 (2003).
  - [16] H. Lippert, J. Manz, M. Oppel, G. K. Paramonov, W. Radloff, H.-H. Ritze, and V. Stert, Physical Chemistry Chemical Physics **6**, 4283 (2004).
  - [17] P. Saalfrank, T. Vazhappilly, S. Beyvers, G. K. Paramonov, and T. Klamroth, Surface Science Proceedings of the 11th International Workshop on Desorption Induced by Electronics Transitions (DIET-11), Berlin, Germany, March, 11-15th, 2007 Proceedings of the 11th International Workshop on Desorption Induced by Electronics Transitions (DIET-11), **602**, 3153 (2008).
  - [18] P. Nuernberger, D. Wolpert, H. Weiss, and G. Gerber, Physical Chemistry Chemical Physics **14**, 1185 (2011).
  - [19] G. Vogt, G. Krampert, P. Niklaus, P. Nuernberger, and G. Gerber, Physical Review Letters **94**, 068305 (2005).
  - [20] M. J. Shu, P. Zalden, F. Chen, B. Weems, I. Chatzakis, F. Xiong, R. Jeyasingh, M. C. Hoffmann, E. Pop, H.-S. P. Wong, M. Wuttig, and A. M. Lindenberg, Applied Physics Letters **104**, 251907 (2014).
  - [21] T. Kampfrath, K. Tanaka, and K. A. Nelson, Nature Photonics **7**, 680 (2013).
  - [22] Y. Ma, M. Huang, S. Ryu, C. W. Bark, C.-B. Eom, P. Irvin, and J. Levy, Nano letters **13**, 2884 (2013).
  - [23] S. I. Mityukovskiy, Y. Liu, B. Prade, A. Houard, and A. Mysyrowicz, Applied Physics Letters **102**, 221107 (2013).
  - [24] M. Sato, T. Higuchi, N. Kanda, K. Konishi, K. Yosh-

- ioka, T. Suzuki, K. Misawa, and M. Kuwata-Gonokami, *Nature Photonics* **7**, 724 (2013).
- [25] H. Fuser and M. Bieler, *Applied Physics Letters* **102**, 251109 (2013).
- [26] N. Stojanovic and M. Drescher, *Journal of Physics B: Atomic, Molecular and Optical Physics* **46**, 192001 (2013).
- [27] Z. Wu, A. S. Fisher, J. Goodfellow, M. Fuchs, D. Daranciang, M. Hogan, H. Loos, and A. Lindenberg, *Review of Scientific Instruments* **84**, 022701 (2013).
- [28] D. Daranciang, M. J. Highland, H. Wen, S. M. Young, N. C. Brandt, H. Y. Hwang, M. Vattilana, M. Nicoul, F. Quirin, J. Goodfellow, T. Qi, I. Grinberg, D. M. Fritz, M. Cammarata, D. Zhu, H. T. Lemke, D. A. Walko, E. M. Dufresne, Y. Li, J. Larsson, D. A. Reis, K. Sokolowski-Tinten, K. A. Nelson, A. M. Rappe, P. H. Fuoss, G. B. Stephenson, and A. M. Lindenberg, *Physical Review Letters* **108**, 087601 (2012).
- [29] T. Qi, Y.-H. Shin, K.-L. Yeh, K. A. Nelson, and A. M. Rappe, *Physical Review Letters* **102**, 247603 (2009).
- [30] F. Enderli and T. Feurer, *Applied Physics Letters* **103**, 061903 (2013).
- [31] Q. Chao-Chao, L. Yu-Zhu, Z. Xian-Zhou, and L. Yu-Fang, *Chinese Physics Letters* **30**, 023301 (2013).
- [32] H. Ogasawara and D. a. N. N. (Anders), *Ultrafast coherent control and characterization of surface reactions using FELs*, Tech. Rep. (United States. Department of Energy, 2005).
- [33] B. D. Patterson, J. Sa, C. P. Hauri, C. Vicario, C. Ruchert, I. Czekaj, R. Gehrig, H. C. Sigg, J. A. van Bokhoven, B. Pedrini, and others, *CHIMIA international Journal for Chemistry* **65**, 323 (2011).
- [34] G. Murgida, D. Wisniacki, P. Tamborenea, and F. Borondo, *Chemical Physics Letters* **496**, 356 (2010).
- [35] B. S. Jursic, *Journal of Molecular Structure: THEOCHEM* **428**, 41 (1998).
- [36] J. Makarewicz and T.-K. Ha, *Journal of Molecular Structure: THEOCHEM* **315**, 149 (1994).
- [37] P. Von Ragu Schleyer, A. Sawaryn, A. E. Reed, and P. Hobza, *Journal of computational chemistry* **7**, 666 (1986).
- [38] Y. Wang, X. Hong, J. Liu, and Z. Wen, *Journal of Molecular Structure: THEOCHEM* **369**, 173 (1996).
- [39] R. Essers, J. Tennyson, and P. Wormer, *Chemical Physics Letters* **89**, 223 (1982).
- [40] G. Brocks and J. Tennyson, *Journal of Molecular Spectroscopy* **99**, 263 (1983).
- [41] B. Bak, *The Journal of Chemical Physics* **52**, 764 (1970).
- [42] Z. K. Ismail, *The Journal of Chemical Physics* **57**, 5137 (1972).
- [43] J. van Vaals, W. Meerts, and A. Dymanus, *Chemical Physics* **82**, 385 (1983).
- [44] X. Andrade, J. Alberdi-Rodriguez, D. A. Strubbe, M. J. T. Oliveira, F. Nogueira, A. Castro, J. Muguerza, A. Arruabarrena, S. G. Louie, A. Aspuru-Guzik, A. Rubio, and M. A. L. Marques, *Journal of Physics: Condensed Matter* **24**, 233202 (2012).
- [45] A. Castro, H. Appel, M. Oliveira, C. A. Rozzi, X. Andrade, F. Lorenzen, M. a. L. Marques, E. K. U. Gross, and A. Rubio, *physica status solidi (b)* **243**, 2465 (2006).
- [46] M. A. Marques, A. Castro, G. F. Bertsch, and A. Rubio, *Computer Physics Communications* **151**, 60 (2003).
- [47] M. J. Frisch, G. W. Trucks, H. B. Schlegel, G. E. Scuseria, M. A. Robb, J. R. Cheeseman, G. Scalmani, V. Barone, B. Mennucci, G. A. Petersson, H. Nakatsuji, M. Caricato, X. Li, H. P. Hratchian, A. F. Izmaylov, J. Bloino, G. Zheng, J. L. Sonnenberg, M. Hada, M. Ehara, K. Toyota, R. Fukuda, J. Hasegawa, M. Ishida, T. Nakajima, Y. Honda, O. Kitao, H. Nakai, T. Vreven, J. A. Montgomery, Jr., J. E. Peralta, F. Ogliaro, M. Bearpark, J. J. Heyd, E. Brothers, K. N. Kudin, V. N. Staroverov, R. Kobayashi, J. Normand, K. Raghavachari, A. Rendell, J. C. Burant, S. S. Iyengar, J. Tomasi, M. Cossi, N. Rega, J. M. Millam, M. Klene, J. E. Knox, J. B. Cross, V. Bakken, C. Adamo, J. Jaramillo, R. Gomperts, R. E. Stratmann, O. Yazyev, A. J. Austin, R. Cammi, C. Pomelli, J. W. Ochterski, R. L. Martin, K. Morokuma, V. G. Zakrzewski, G. A. Voth, P. Salvador, J. J. Dannenberg, S. Dapprich, A. D. Daniels, . Farkas, J. B. Foresman, J. V. Ortiz, J. Cioslowski, and D. J. Fox, "Gaussian09 Revision D.01," (2009), gaussian Inc. Wallingford CT 2009.
- [48] J. J. Larsen, H. Sakai, C. P. Saffan, I. Wendt-Larsen, and H. Stapelfeldt, *The Journal of Chemical Physics* **111**, 7774 (1999).
- [49] M. Machholm and N. E. Henriksen, *Physical Review Letters* **87**, 193001 (2001).
- [50] M. Leibscher, I. S. Averbukh, and H. Rabitz, *Physical Review Letters* **90**, 213001 (2003).
- [51] S. Fleischer, Y. Khodorkovsky, Y. Prior, and I. S. Averbukh, *New Journal of Physics* **11**, 105039 (2009).
- [52] Y. Khodorkovsky, K. Kitano, H. Hasegawa, Y. Ohshima, and I. S. Averbukh, *Physical Review A* **83**, 023423 (2011).
- [53] M. Lapert and D. Sugny, *Physical Review A* **85**, 063418 (2012).
- [54] M. Lemesko, R. V. Krems, J. M. Doyle, and S. Kais, *Molecular Physics* **111**, 1648 (2013).
- [55] J. Perdew and A. Zunger, *Physical Review B* **23**, 5048 (1981), wOS:A1981LR24700023.
- [56] N. Troullier and J. L. Martins, *Physical Review B* **43**, 1993 (1991).
- [57] J. P. Perdew, K. Burke, and M. Ernzerhof, *Physical Review Letters* **77**, 3865 (1996).
- [58] J. C. Slater, *Physical review* **81**, 385 (1951).
- [59] S. H. Vosko, L. Wilk, and M. Nusair, *Canadian Journal of Physics* **58**, 1200 (1980).
- [60] A. Becke, *Physical Review A* **38**, 3098 (1988), wOS:A1988Q146900044.
- [61] C. Lee, W. Yang, and R. Parr, *Physical Review B* **37**, 785 (1988), wOS:A1988L976200011.
- [62] A. Becke, *Journal of Chemical Physics* **98**, 5648 (1993), wOS:A1993KV99700048.
- [63] R. Krishnan and J. A. Pople, *International Journal of Quantum Chemistry* **14**, 91 (1978).
- [64] M. Head-Gordon, R. J. Rico, M. Oumi, and T. J. Lee, *Chemical Physics Letters* **219**, 21 (1994).
- [65] M. E. Casida, C. Jamorski, K. C. Casida, and D. R. Salahub, *The Journal of Chemical Physics* **108**, 4439 (1998).
- [66] R. Ditchfield, W. J. Hehre, and J. A. Pople, *The Journal of Chemical Physics* **54**, 724 (1971).
- [67] W. Magnus, *Communications on Pure and Applied Mathematics* **7**, 649 (1954).
- [68] Y. Saad, *SIAM Journal on Numerical Analysis* **29**, 209 (1992).
- [69] X. Andrade, A. Castro, D. Zueco, J. L. Alonso, P. Echenique, F. Falceto, and . Rubio, *Journal of chem-*

- ical theory and computation **5**, 728 (2009).
- [70] J. R. Dormand and P. J. Prince, Journal of Computational and Applied Mathematics **6**, 19 (1980).
- [71] J. C. Lagarias, J. A. Reeds, M. H. Wright, and P. E. Wright, SIAM journal on optimization **9**, 112 (1998).
- [72] R. H. Byrd, J. C. Gilbert, and J. Nocedal, Mathematical Programming **89**, 149 (2000).